X-ray analysis of a magnesium alloy expected to be a useful lightweight material

Akimitsu Nezu*, Wataru Matsuda**, and Junichi Sato***

1. Introduction

Weight saving is an important challenge for various industries, including transportation (automotive, aeronautical, or bullet-train manufacturing), electronic devices, and intelligent robotics. Finding lighter-weight materials is, therefore, a popular research subject because of its potential impact on peoples' daily life. This is especially true in the modern automotive industry, where better fuel economy and reduction of CO_2 emissions are now even more important requirements in technology development as the global number of cars owned is expected to keep growing.

A significant trend when making parts is to replace steel with a light metal or a high-strength resin. Magnesium is regarded as a prospective next-generation high-performance material. In fact, the Nonferrous Metals Division of the Japan Ministry of Economy, Trade and Industry has published a report titled "Nonferrous Metal Industrial Strategy 2016"[(1)], which proposes a marketing plan for these light metals, including magnesium.

This article demonstrates examples of multifaceted non-destructive analyses on raw and surface-treated AZ31B, a representative magnesium alloy, using laboratory X-ray analyzers, which are useful non-destructive analysis tools.

2. Magnesium Alloys

2.1. Properties of magnesium

Magnesium (Mg) has the smallest density among the metal materials available for industrial use. Its specific weight of 1.7 is smaller than those of aluminum (2.5), titanium (4.5), or iron (7.9)[(2)]. It also has a higher specific strength (=tensile strength/density) and a higher specific rigidity (=elastic modulus/density) than those of many high-strength resins, making it suitable for structural/industrial use. In addition, it has the best vibration absorption among industrial metal materials, as well as being good in recyclability, castability, dimensional stability, dent resistance, machinability, heat dissipation, electromagnetic shielding, bio-compatibility and other factors.

On the other hand, magnesium has the lowest standard electrode potential among all industrial metals; thus, it is chemically active and susceptible to corrosion. Table 1 shows the standard electrode potential values for representative industrial metals[(3)].

Table 1. Std. electrode potential of industrial metals.

Element, Atomic umber	Reaction	Std. electrode potential [V]
Mg, 12	$Mg^{2+}+2e^- \rightarrow Mg$	−2.36
Al, 13	$Al^{3+}+3e^- \rightarrow Al$	−1.70
Ti, 22	$Ti^{2+}+2e^- \rightarrow Ti$	−1.63
Fe, 26	$Fe^{2+}+2e^- \rightarrow Fe$	−0.44
Au, 79	$Au^{3+}+3e^- \rightarrow Au$	+1.50

Corrosion of magnesium is known to be accelerated significantly by transition-metal impurities, including Fe, Co, Ni and Cu even at low concentrations. In the case of AZ91D alloy, for example, the critical impurity concentration limits are defined as no more than 50 ppm for Fe, 20 ppm for Co, 20 ppm for Ni, and 300 ppm for Cu[(3)].

Another weak point of magnesium is its low plastic workability, especially at room temperature. This comes from its hexagonal close packed (hcp) crystal structure, which has a limited number of slip systems. Table 2 shows the main slip systems of different crystal structures. It is seen that the hcp structure has no more than 3 slip systems (1 plane × 3 directions), while body centered cubic (bcc) and face centered cubic (fcc) structures, which are the structures of Fe, have 12 slip systems (Fig. 1). The ductility of magnesium, however, increases rapidly with temperature. It is known that the workability of magnesium in hot rolling or hot exclusion becomes comparable to that of aluminum at around 300°C[(6)].

Improving corrosion resistance, workability and other mechanical characteristics is essential for promoting

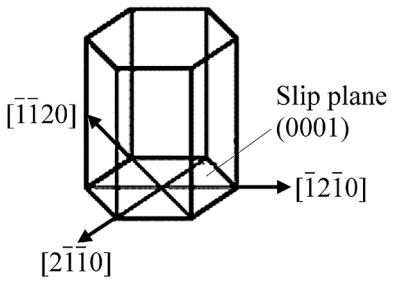

Fig. 1. Slip systems of magnesium crystal.

* Application Laboratory, X-ray Instruments Division, Rigaku Corporation.
** SBU WDX, X-ray Instruments Division, Rigaku Corporation.
*** SBU X-ray Imaging, X-ray Instrument Division, Rigaku Corporation.

Table 2. Slip systems of different structures.

Crystal structure	Slip plane	Slip direction	Num. of slip systems
bcc	{110}	$\langle 1\bar{1}1 \rangle$	6×2=12
fcc	{111}	$\langle 1\bar{1}0 \rangle$	4×3=12
hcp	{0001}	$\langle \bar{1}\bar{1}20 \rangle$	1×3=3

the industrial implementation of magnesium. Possible measures against corrosion include surface treatments such as chemical conversion coating, anodization, thermal spray process, and metal plating, as well as alloying by adding Al, Zn, Mn, Si, Y, or other rare-earth elements. Alloying is also considered as a potential measure to improve the workability by adding Al, Cu, Ca, Th, Zr, Sn, or Y[2),7)]. Previous studies show that the mechanism of characteristics improvements involves the effects of smaller crystallite size or higher randomness in crystal orientation realized by these processes[8)–10)].

2.2. AZ31B alloy

AZ31B is a representative industrial magnesium alloy mainly used for wrought products. While its strength is modest among other magnesium alloys, it has excellent moldability.

The widely-used nomenclature of magnesium alloys is defined in ASTM standards, while another definition system is given in Japanese Industrial Standards (JIS). For the case of AZ31B in the ASTM nomenclature, the letter "A" and "Z" mean the added elements with the highest and the second-highest concentrations, "Al" and "Zn" in this case. The following "3" and "1" mean the concentrations of these two elements in [wt.%]. The last letter "B" is a serial identifier added to distinguish different alloys that otherwise would have had identical names[11)].

2.3. Chemical conversion coating

A chemical conversion coating is a surface treatment for metals where a film of insoluble compounds is formed chemically on the metal surface by immersing the metal in a solution to improve corrosion resistance or paint adhesiveness. The technique is widely used for its versatility, simplicity, and low cost.

Until recently, a popular chemical conversion coating for magnesium was chromate treatment. The process uses a solution of chromic anhydride or dichromate, both of which include hexavalent chromium ions. The process is now being replaced by chromium-free conversion coating processes because of increased social requirements for reducing the use of environmentally hazardous substances or, more specifically, the establishment of the RoHS directives, which limit the use of six hazardous materials (Pb, Hg, Cd, Cr^{6+}, PBB, and PBDE) in producing electronic devices. The new techniques include those based on phosphates, oxalates, permanganic acid or stannates, while the phosphate-based process is most popular in treating magnesium alloys. Specifically, *X*-calcium phosphate (*X*=Mn, V) coating is widely used for this purpose. The manganese-calcium phosphate coating is especially excellent in corrosion resistance, electric conductivity and paint adhesiveness[12),13)].

2.4. Samples

A raw plate of the magnesium alloy and another plate with a chemical conversion coating were used for the measurements (Fig. 2) in order to identify the effect of the coating by comparing the X-ray analysis results between these samples.

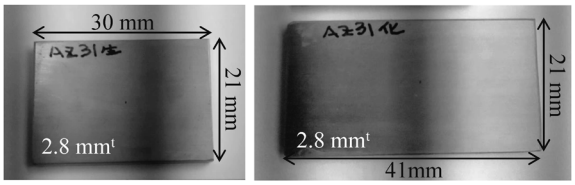

Fig. 2. The raw plate (left) and the plate with a chemical conversion coating (right).

The conducted experiments include identification of the constituent elements, quantification of the alloy components, coating-thickness measurement, crystallinity evaluation, crystal-structure identification, crystallite-size analysis, lattice-strain analysis within the crystallites, surface mapping of the inter-crystallite residual stress, texture or crystal-orientation analysis, and internal mechanical-structure imaging of the alloys.

3. Multifaceted X-ray Analyses

3.1. X-ray diffraction

X-ray diffraction is an analytical technique that can examine the crystal phases in a sample nondestructively. The technique is based on Bragg's law ($2d\sin\theta=n\lambda$), where d is the interval between the lattice planes, θ is the Bragg angle (half of the diffraction angle, 2θ), and λ is the wavelength of the characteristic X-rays. The technique is widely used in various industries as well as in academia for its ability to analyze samples in powder, liquid, fiber, or gel forms—as well as in bulk form—easily and quickly.

We used two different diffraction systems, each of which has different characteristics. One is the SmartLab system, a θ–θ multipurpose diffractometer capable of switching its optical system into various different configurations. The other is the stress analyzer, AutoMATE II. This system can perform precise analyses on a small spot on the sample surface (Fig. 3).

The general X-ray diffraction measurements were conducted using the SmartLab with a Cu X-ray tube (2.2 kW) and a HyPix-3000 pixel array detector, which can switch between 0-, 1-, and 2-dimensional modes. These include $2\theta/\theta$-scanning wide-angle diffraction (1D/2D), 2θ-scanning grazing-incidence diffraction (0D), crystallite-size and lattice strain analysis (1D), and pole-figure measurement (2D). The residual stress analyses were done on 9 spots arranged around the

Fig. 3. SmartLab (left) and AutoMATE II (right).

center of the sample at a 5 mm interval using the AutoMATE II with a Cr X-ray tube (2.0 kW) and a D/teX Ultra 1000 1-dimensional detector.

3.2. X-ray fluorescence analysis

X-ray fluorescence analysis is a non-destructive technique used to identify and quantify the constituent elements of a sample. It is widely used especially in steel and nonferrous-metal industries, as it can be applied to various sample forms just like X-ray diffraction[14]. The technique is based on the secondary X-ray emission of the sample elements. This occurs when X-rays with an energy higher than the specific threshold of the element irradiate the sample, exciting and expelling an inner-shell electron of the element, so that an outer-shell electron falls into the vacant inner-shell orbital. This transition releases energy corresponding to the energy-level difference between the two orbitals in the form of X-rays. Thus, the fluorescent X-rays have an energy spectrum specific to the element, and their intensity is proportional to the concentration of the elements in the sample.

There are two types of X-ray fluorescence analyses. One is wavelength dispersive X-ray fluorescence (WDXRF) analysis, which uses an analyzing crystal to measure the X-ray intensity in a narrow wavelength band at a time, and scans the wavelength range to obtain the whole spectrum. This is suitable for high-precision measurements, as it has higher sensitivity to light elements and higher energy resolution. The other type is energy dispersive X-ray fluorescence (EDXRF) analysis, which uses a silicon drift detector with energy-discriminating capability. It allows a shorter measurement time and a smaller instrument size.

While the calibration curve method is widely used in quantitative analyses, a unique technique, called the fundamental parameter (FP) method, can perform quantitative analyses without standard samples by using a sensitivity library for different elements. This method is effective where standard samples are not readily available. Using this method, Matsuda *et al.* obtained concentrations that are in good agreement with the certified values for the elements (not only major ingredients such as Al, Mn, Si, and Zn but also trace elements such as Fe, Ni, Cu, Sn, and Pb) in a certified standard magnesium-alloy samples made by MBH[16].

Compared with traditional wet-chemical analysis, X-ray fluorescence analysis has the advantage that it does not require time-consuming sample preparations, including making a sample solution and the separation and concentration of the target ingredients. Also, it is more suitable for screening when detailed sample information is not available because of its nondestructive nature and its capability of conducting analyses without standard samples.

In this work, the WDXRF instrument ZSX Primus IV was used (Fig. 4). First, a wide-range (oxygen to curium) qualitative element identification was performed. Then FP quantitative analysis determined the composition of the raw plate. Using the obtained alloy composition, the amount of chemical conversion coating on the coated plate was calculated.

Fig. 4. ZSX Primus IV.

3.3. X-ray computed tomography analysis

X-ray computed tomography (CT) analysis is a technique used to nondestructively observe the 3-dimensional internal structure of a material. The technique is based on the difference in X-ray absorption between materials with different densities. The sample is rotated 360° to obtain X-ray transmission images at many different rotation angles. The obtained image data are processed to reconstruct and visualize the internal 3D structure, including inclusions or voids in the sample.

There are two major application fields for X-ray CT: medical and industrial. For X-ray CT instruments for medical applications, whose target is human bodies, the required spatial resolution is typically 100 μm–1.0 mm. For industrial applications, on the other hand, the required resolution varies over a wider range, such as 0.1 μm–1 mm, because the targets to be examined range from large parts to the internal structure of smaller samples to micro-structures of samples[17]. As advancements in CPUs and GPUs enhance data processing, the use of the X-ray CT technique has rapidly become more popular in various stages in manufacturing businesses, including R&D, quality control, and on-site inspection.

In this work, the desktop X-ray CT instrument CT LAB HX was used (Fig. 5). A typical measurement condition is to use a tungsten tube (130 kV × 30 μA = 3.9 W), and to take 2400 projections, each consisting of a composite of 9 images. A 1.0 mm^t Al plate was used as the X-ray filter. Reconstructed 3D image processing was done using VGSTUDIO MAX ver.3.4.5 software by Volume Graphics.

Fig. 5. CT Lab HX.

4. Results and Discussion

4.1. X-ray diffraction analyses results

4.1.1. X-ray diffraction profiles (0D/1D/2D)

Figure 6 shows the wide-angle $2\theta/\theta$ diffraction profiles of the two samples ($2\theta/\theta$ = 18.0–145.0°, 5°/min, 1D-scan). Performing qualitative analysis using the ICDD-PDF2 database, the major component was identified as Mg–(Al/Zn) alloy for both the raw and coated plates. The analysis also suggested that the trace component was an Al–Mn intermetallic compound (Al_8Mn_5) for both samples, but this is not conclusive because the number and intensities of the obtained peaks were limited. Although the elemental analysis (Table 2 in Section 4.2) gave a consistent result, the Al–Mn intermetallic compound should remain as a strong candidate for the trace phase identity.

It should be noted that the raw and coated plates give an identical set of crystal peaks. This suggests either that the chemical conversion coat is not a crystalline substance or that the coat thickness is too thin to observe its crystalline features. It is also notable that there is a significant difference in the shapes of the peaks obtained from the raw and coated plates; the coated plate gives narrower (sharper) peaks than the raw plate (Fig. 7). This suggests that the crystallite size becomes larger during the chemical conversion coating process.

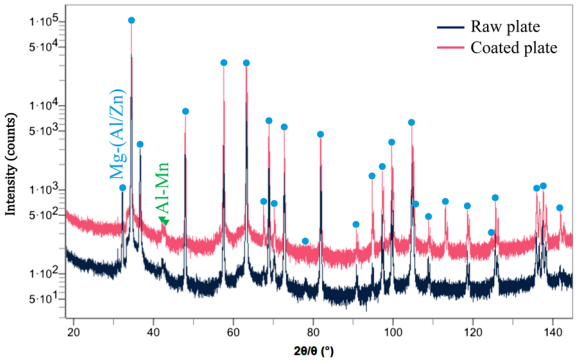

Fig. 6. Wide-angle $2\theta/\theta$ diffraction profiles, $2\theta/\theta$ = 18.0–145.0°.

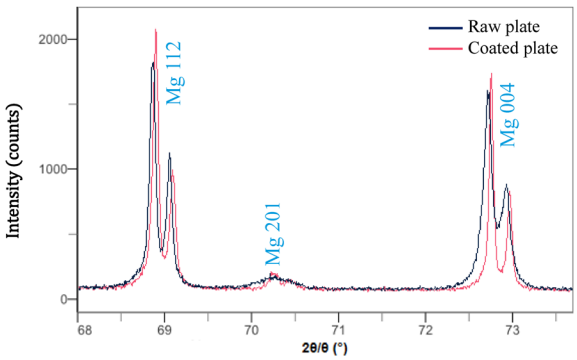

Fig. 7. Magnified $2\theta/\theta$ profiles, $2\theta/\theta$ = 68.0–73.7°.

Grazing-incidence X-ray diffraction (GI-XRD) measurements were conducted for the samples. This method is an X-ray diffraction configuration where the incidence angle is fixed at a small angle, scanning only the 2θ-axis. The small incident angle keeps the penetration depth of the X-rays small, thus allowing selective measurement of the surface part of the sample or of a film formed on the sample surface. Figure 8 shows the obtained profiles at an incident angle of 0.5° (2θ = 20.0–120.0°, 0.25°/min, 0D-scan).

No sharp peaks originated from the coated plate; only substrate peaks. At around 2θ = 30°, however, a broad halo appears that is not seen in the raw-plate profile. This indicates that the chemical conversion coat is thinner than the penetration depth of the X-rays and that it is non-crystalline. It is known that the nature of a chemical conversion coat can vary depending on the type of the substrate, solution, process temperature, and other factors[18]. Formation of non-crystalline coat was also reported by Tsunakawa *et al.*[12].

We carefully looked for MgO peaks because magnesium is known to react with oxygen easily, but no such peaks were observed.

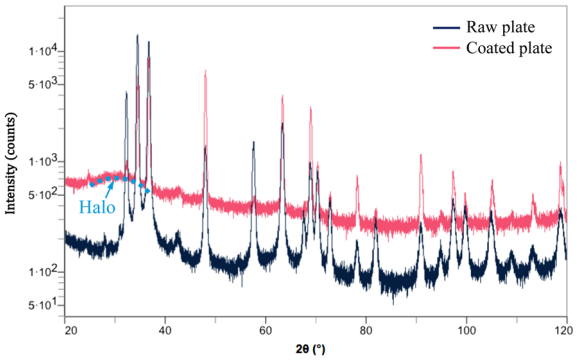

Fig. 8. GI-XRD method 2θ profiles with ω = 0.5°, 2θ = 20.0–120.0°.

Wide-angle X-ray diffraction using the 2D-scan capability was also conducted. This method can visualize the 2D image of the Debye rings, thus it provides visual information on the crystallite size and the existence of texture. Figure 9 shows the obtained profiles ($2\theta/\theta$ = 18.0–145.0°, 10°/min, 2D-scan).

It is seen that the intensity uniformity along the Debye rings is lower for the coated plate than for the raw plate. This suggests that the crystallite size becomes larger after the chemical conversion coating process. This is consistent with the result of the peak-width comparison (Fig. 7). It should be noticed that Mg 002 reflection is especially strong compared to other peaks for both raw and coated plates. This suggests that the substrate has a 001 preferred orientation regardless of the existence of the chemical conversion coat.

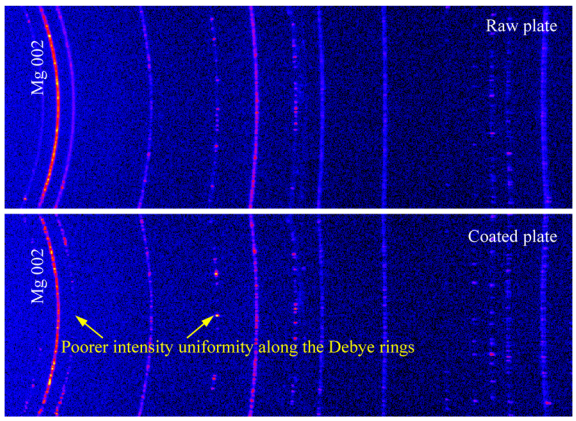

Fig. 9. 2D wide-angle $2\theta/\theta$ profiles, $2\theta/\theta = 18.0$–$145.0°$.

4.1.2. Crystallite-size and lattice-strain analyses (1D) results

Crystallite size and lattice strain were analyzed using the Williamson–Hall (W–H) method[19]. In this method, the peak width β is assumed to be the sum of the contributions from the crystallite size and the lattice strain, β_D and β_S, respectively, as in the basic formulae for the W–H method (Eq. (1)). Here, β is the integral width of a diffraction peak in the profile after correcting for instrumental broadening, D is the crystallite size, ε is the lattice strain, θ is the Bragg angle (half of the diffraction angle, 2θ), and λ is the wavelength of the incident X-rays.

$$\beta = \beta_D + \beta_S = \frac{\lambda}{D\cos\theta} + 2\varepsilon\tan\theta$$
$$\beta\frac{\cos\theta}{\lambda} = 2\varepsilon\frac{\sin\theta}{\lambda} + \frac{1}{D}$$
$$\Delta K = \varepsilon K + \frac{1}{D} \qquad (1)$$

One can draw a plot with the scattering vector, $K = (2\sin\theta)/\lambda$, along the x-axis and the peak width, $\Delta K = (\beta\cos\theta)/\lambda$, along the y-axis. From the linear regression of the data, the lattice strain, ε, and crystallite size, D, are estimated from the slope and the y-intercept of the regression line, respectively.

Figure 10 shows the Williamson–Hall plots of the data obtained from the samples. Obtained results are $D = 276 \pm 78$ nm, $\varepsilon = 0.048 \pm 0.005\%$ for the raw plate, and $D = 358 \pm 245$ nm, $\varepsilon = 0.043 \pm 0.010\%$ for the coated plate. These mean that the coated plate has a larger crystallite size and a smaller lattice strain than the raw plate.

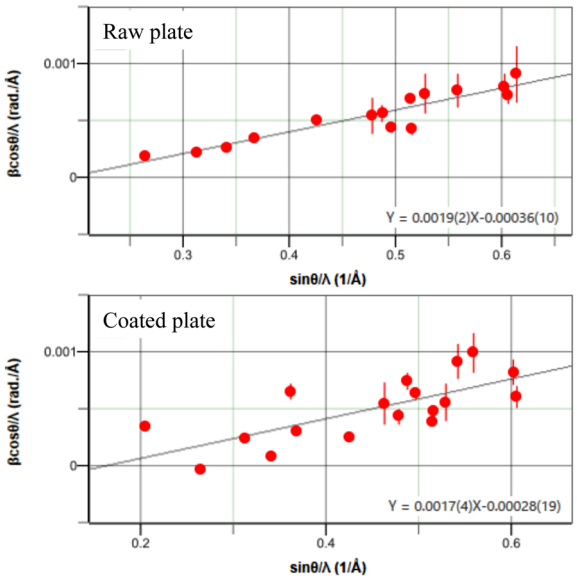

Fig. 10. Williamson–Hall plots.

The correction for instrumental broadening was done using a LaB_6 standard powder (NIST-SRM660c).

4.1.3. Residual stress analysis (1D) results

The $\sin^2\psi$ technique is a widely used method for measuring the residual stress of a polycrystalline sample by measuring the inter-plane distance, d, from the diffraction of a specific index at various angles, ψ, where ψ is the angle between the surface normal, N, and the normal to the diffracting lattice planes, N'.

The advantage of this method is its small error propagation. This allows strain analysis even when the interlayer distance under no strain, d_0, is not known. In this method, σ_x, the residual stress along the ψ direction, is expressed as Eq. (2), where K is the stress constant defined in Eq. (3). Here, E is Young's modulus, ν is Poisson's ratio, and θ_0 is the diffraction angle under no strain. One can draw a plot with $\sin^2\psi$ along the x-axis and 2θ along the y-axis. This is called a $\sin^2\psi$ plot. The slope of its linear regression multiplied by the constant K gives the residual stress.

$$\sigma_X = K\frac{\partial(2\theta)}{\partial(\sin^2\psi)} \qquad (2)$$

$$K = -\frac{E}{2(1+\nu)}\cot\theta_0 \qquad (3)$$

Diffraction measurements were conducted using Mg 104 as the diffraction plane and using a $\phi 1$ mm collimator. The angle ψ was scanned in the range of 0–45°. The stress constant of the magnesium alloy was not a measured by, for example, a four-point bending test this time. Instead, we used the literature value for pure magnesium, $K = -70.61$ MPa/°, for convenience. For the Young's modulus, Poisson's ratio, and the diffraction angle under no strain, $E = 44{,}500$ MPa, $\nu = 0.29$, and $2\theta_0 = 153.6°$ were adopted, respectively.

Figure 11 shows the obtained residual stress distributions. It is seen that the coated plate has a

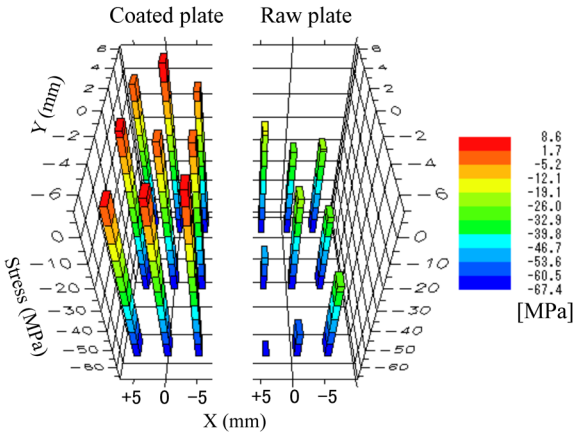

Fig. 11. Residual stress distributions obtained using the Mg 104 diffraction.

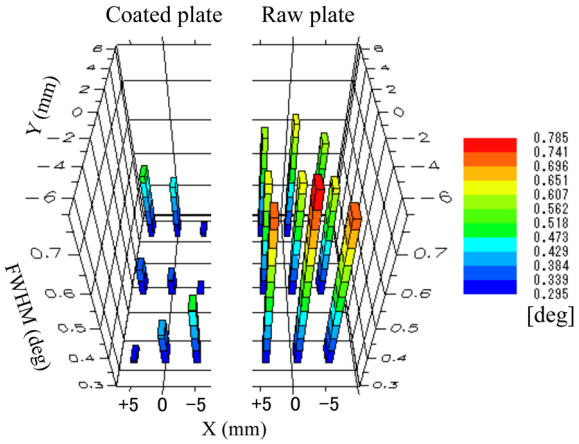

Fig. 12. FWHM distributions of the Mg 104 peak at ψ=0°.

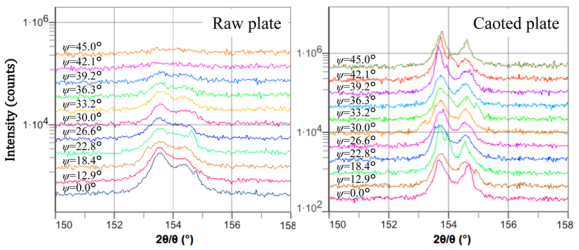

Fig. 13. Peak shift of the Mg 104 diffraction at ψ=0–45°.

tensile stress (positive σ) over the measured area, while the raw plate has a compression stress (negative σ). The average stress over the 9 measurement points was −36.1±3.9 MPa for the raw plate, and 2.9±2.3 MPa for the coated plate.

Figure 12 shows the distribution of the full width at half maximum (FWHM) of the peak. The coated plate gives smaller peak widths than the raw plate. This is consistent with the result shown in Fig. 7. The average FWHM over the 9 points are 0.66° for the raw plate and 0.38° for the coated plate.

Figure 13 shows the observed peak shift at different ψ angles. It is seen that the Mg 104 peak intensity decreases with ψ for the raw plate, while it remains almost constant for the coated plate. This result suggests that the texture is changed by the chemical conversion coating, increasing the randomness of the crystal orientation in the sample.

4.1.4. Pole figure measurement (2D) results

Figure 14 shows the obtained 002, 102, and 110 pole figures for the two samples, and Fig. 15 shows the ND inverse pole figures.

It is seen in the 002 pole figures in Fig. 14 that both the raw and coated plates have a pole near the center of their 002 figures, indicating both samples have a 001 preferred orientation. The coated plate, however, has a weaker normalized intensity of this pole than the raw plate. This difference is also seen in Fig. 15, suggesting the crystal orientation of the substrate becomes more random by the chemical conversion coating process. It was also found that the Mg 002 pole was tilted from the pole figure center (the surface normal) by $\Delta\alpha$=20–25° for both the raw and coated plates.

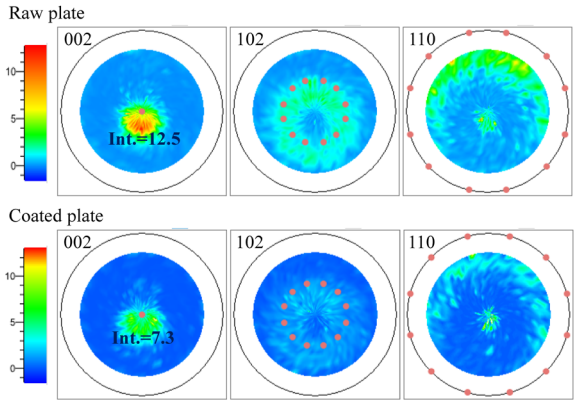

Fig. 14. 002, 102, and 110 pole figures.

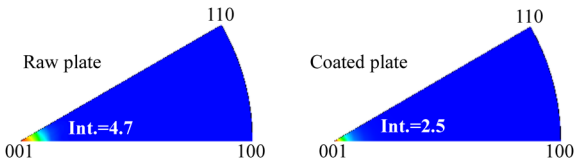

Fig. 15. ND inverse pole figures.

An orientation distribution function (ODF) analysis was conducted on the 001 orientation components of the samples. This method is used to quantitatively evaluate the three-dimensional crystal orientation distribution by calculating a so-called crystal orientation distribution function from the measured pole figures of multiple diffraction planes[20].

The result is shown in Fig. 16. It is seen that the 001 orientation component is reduced in the coated plate. Here, it is assumed that other minor orientation components are included in the random components.

4.2. X-ray fluorescence analysis results

Figure 17 shows the obtained WDXRF spectra of the raw and coated plates. The spectrum of the coated plate clearly shows P, Ca, and Mn peaks, which are not observed in the raw plate. This indicates that manganese-calcium phosphate film is formed on the coated plate. The fluorine (F) peak was also detected in the coated plate spectrum, suggesting the formation of fluorine compounds in the film that prevents dissolution

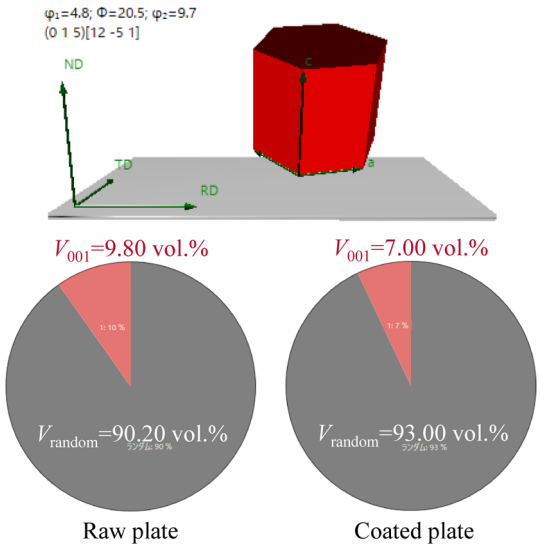

Fig. 16. Volume fraction of the 001 orientation component.

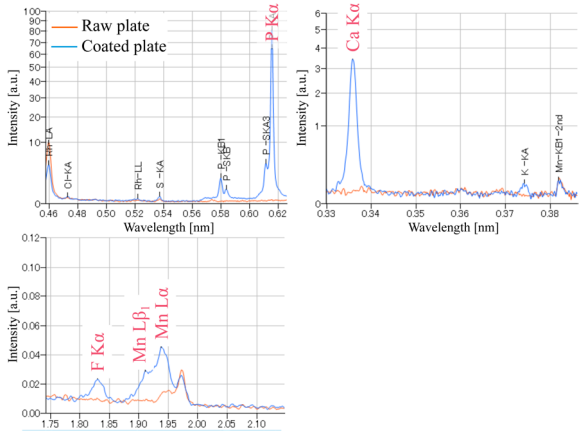

Fig. 17. Obtained WDXRF spectra.

of the magnesium alloy surface[3].

Table 3 shows the obtained elemental composition of the raw plate. Using the ZSX Guidance software, which can identify the material type of the sample by comparing the obtained analysis results with a material standard database, the magnesium alloy was determined to be of the AZ31 series. It should be noted that an Fe concentration of as low as 0.0056 mass% (56 ppm) was detected, especially when we recall that Fe, Co, Ni, and Cu impurity levels need to be controlled and managed strictly, and that ppm-level sensitivity is needed as mentioned in Section 2.4.

Table 3. Composition of the raw plate measured by WDXRF.

Element	Concentration [mass%]	Analytical line
Mg	95.48	Mg Kα
Al	3.01	Al Kα
Zn	0.972	Zn Kα
Mn	0.491	Mn Kα
Si	0.0351	Si Kα
Fe	0.0056	Fe Kα

Table 4 shows the WDXRF analysis result of the chemical conversion coat layer of the coated plate. The element types and the amount of the coat were analyzed using the obtained composition of the raw plate as fixed values for the substrate. The result shows the coat layer includes many types of elements such as P, Ca, Mn, or Al. It is noticeable that light elements such as oxygen (O) and fluorine (F), as well as chlorine (Cl), all of which affect the coat properties, were also detected by this technique.

Table 4. Constituent elements and their amount in the chemical conversion coat of the coated plate.

Element	Adhesion amount [μg/cm^2]	Analytical line
P	10.4	P Kα
Mn	10.0	Mn Lα
Ca	5.4	Ca Lα
Al	2.8	Al Kα
F	0.37	F Kα
Si	0.10	Si Kα
K	0.07	K Kα
Cl	0.05	Cl Kα
S	0.01	S Kα
O	32.0	O Kα

4.3. X-ray computer tomography results

Figure 18(a) shows the tomograms and 3D volume rendering images. In both the raw and coated plates, multiple small areas with a higher density than the surrounding components were observed as spot inclusions. Each tomogram shows a perpendicular section in different directions, and the intersection of the crossline on each tomogram has the same coordinates. Considering the density difference between the substrate and the spots, the included elements in the substrate, and the fact that the existence of Al–Mn intermetallic compound grains were previously reported in AZ91E alloy[21], these spots are assumed to be an intermetallic compound composed of Al, Zn, and Mn. The X-ray diffraction results shown in Fig. 6 suggests the component of these spots is the Al–Mn compound, Al_8Mn_5. The volume and volume fraction of the high-density spots were calculated to be 0.0689 mm^3 and 0.43% for the raw plate and 0.0452 mm^3 and 0.28% for the coated plate, respectively; the coated plate has a smaller volume of high-density spots than that of the raw plate. Here, the analyzed volume was about 16.5 mm^3 (=2.2 mm × 3.0 mm × 2.5 mm) shown in Fig. 18(b). Considering the effect of beam hardening on the sample surface, 30 pixels from the surface of the analysis area were excluded from the analysis target.

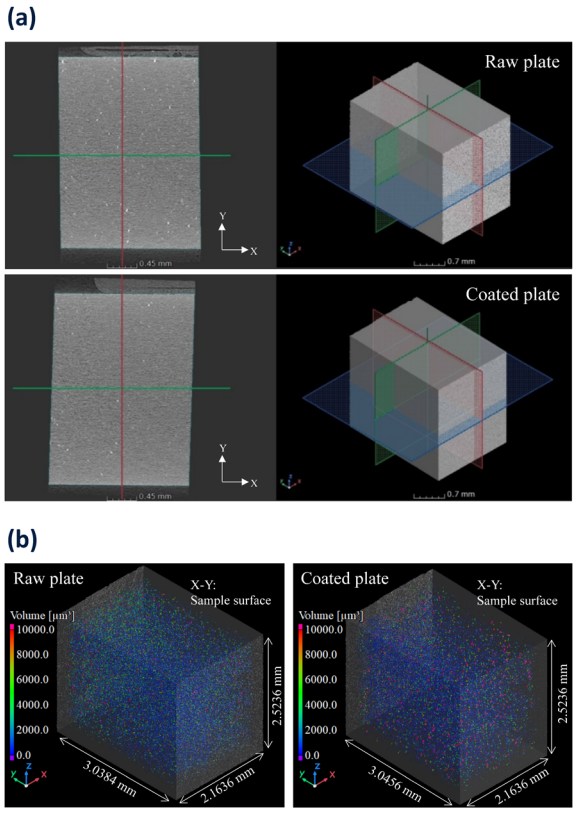

Fig. 18. (a) Tomograms and 3D volume rendering image with crossline. (b) 3D volume rendering image with each volume of high-density spots.

Figure 19 shows the volume-fraction distribution of the high-density spots along the *y*-axis direction in the X–Z plane. In the range from 0.0 mm to 2.7 mm, the raw and coated plates show similar variation trends, while the volume fraction of the coated plate is lower than that of the raw plate over this range. The number of high-density spots was estimated from the histogram data to be 83,442 for the raw plate and 71,494 for the coated plate. It is seen that the number of high-density spots also decreases by the chemical conversion coating process.

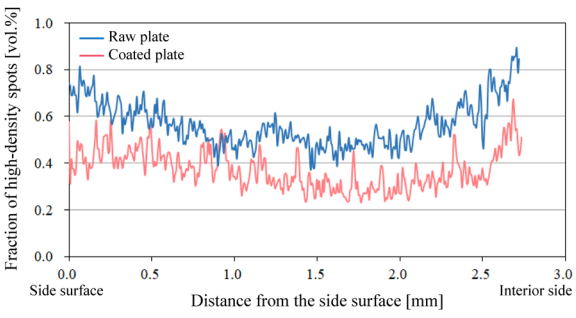

Fig. 19. Volume-fraction distribution of the high-density spots.

4.4. Summary of analysis results

The following findings were obtained from the comparison of the various X-ray analysis results for the raw and chemical conversion coated plates.

1) The substrate material is an AZ31 series magnesium alloy.
2) The conversion coating is a manganese-calcium phosphate compound, contains fluorine compounds, and is non-crystalline.
3) The chemical conversion coating causes the following changes: an increase in (a growth of) crystallite size, a decrease in lattice distortion, a decrease in compressive residual stress, and a decrease in 001 orientation components (randomization of orientation).
4) A trace amount of an Al–Mn intermetallic compound, Al_8Mn_5, is crystallized in the alloy matrix. The fraction of this compound volume decreases with the chemical conversion coating process.

Here, we discuss the changes in item 3) above. Both the major effect and the main purpose of the chemical conversion coating process are to improve the corrosion resistance of magnesium alloys. However, observed growth in crystallite size and reduction of compressive residual stress can have a negative effect on the hardness or the fatigue strength of the material in some cases. The crystal orientation randomization, on the other hand, is expected to improve the plastic workability of the material. Thus, it was found that the chemical conversion coating process has both positive and negative effects on magnesium alloy materials. By clarifying these mechanisms by X-ray analysis, it is thought that the practicality of magnesium alloys as industrial materials can be further enhanced.

Another possible factor that causes these changes is the pretreatments conducted before the chemical conversion treatment. These include alkali degreasing, acid etching, and smut removal using strong alkaline solution. Those may have indirect or additional effects on the differences observed before and after the coating process. A comparison study between the material conditions before and after such pretreatments is necessary to investigate these possible effects.

5. Conclusion

Magnesium alloys are expected to be the next-generation of high-performance lightweight materials. In order to improve their properties for further industrial applications in the future, highly accurate quantitative evaluation techniques are needed. It has been demonstrated that the multifaceted X-ray analysis techniques introduced in this paper can be effective in the purpose of evaluating magnesium alloys.

Acknowledgments

The magnesium alloy used in this analysis was provided by Fuji Light Metal Co., Ltd., and Ms. Minami Sasaki of Fuji Light Metal Co., Ltd. gave us valuable advice and suggestions. We would like to express our deepest gratitude to them.

References

(1) Nonferrous Metals Division of Japan Ministry of Economy, Trade and Industry: *Brief Summary of Nonferrous Metal Industrial Strategy Looking Ahead to 2030* (*2030 Nen wo Misueta Hitetsukinzoku Sangyo Senryaku no Gaiyou*), June 2016 [in Japanese].

(2) K. Yamada: *J. Surf. Finish. Soc. Jpn.* (*Hyomen Gijutsu*), **71** (2020) 3, 224–232 [in Japanese].

(3) M. Hino: *J. Surf. Finish. Soc. Jpn.* (*Hyomen Gijutsu*), **71** (2020) **3**, 205–211 [in Japanese].

(4) J. E. Hillis and K. N. Reichek: *Soc. Auto. Eng.,* (*SAE*) *Tech. Paper*, 860288, (1986), 1–8.

(5) M. Inoue, M. Iwai, K. Matsuzawa, S. Kamado and Y. Kojima: *J. Jpn. Light Metals* (*Keikinzoku*), **48** (1998) 6, 257–262 [in Japanese].

(6) Y. Kojima: *J. Surf. Finish. Soc. Jpn.* (*Hyomen Gijutsu*), **44** (1993) 11, 866–873 [in Japanese].

(7) K. Kubota: *J. Surf. Finish. Soc. Jpn.* (*Hyomen Gijutsu*), **53** (2002) 3, 172–175 [in Japanese].

(8) Y. Sakaoka, S. Kuramoto, H. Kawabata and A. Kurumada: *Light Metals* (*Keikinzoku*), **69** (2019) 7, 332–338 [in Japanese].

(9) D. Tanaka and S. Kamado: *J. Surf. Finish. Soc. Jpn.* (*Hyomen Gijutsu*), **71** (2020) 3, 200–204 [in Japanese].

(10) Y. Chino, X. Huang and K. Suzuki: *J. Jpn. Inst. Met. Mater.*, **81** (2017) 2, 49–54 [in Japanese].

(11) ASTM Standards, B951–11 (2018).

(12) M. Tsunakawa, Y. Shimada, K. Nakamura, K. Kikuchi, T. Matsumura and T. Ishizaki: *J. Jpn. Light Metals* (*Keikinzoku*), **67** (2017) 10, 497–502 [in Japanese].

(13) A. Serizawa: *J. Surf. Finish. Soc. Jpn.* (*Hyomen Gijutsu*), **71** (2020) 3, 233–238 [in Japanese].

(14) H. Takahara: *X-ray Spectroscopy* (*X sen Bunkou Hou*), Ed. by K. Tsuji and Y. Muramatsu, Kodansha, Tokyo, (2018), 93–94 [in Japanese].

(15) M. Ohgaki: *Introduction to Reference-free X-ray Fluorescence Analysis* (*Rifarensu-furii Keikou X sen Bunseki Nyumon*), Ed. by K. Sakurai, Kodansha, Tokyo, (2019), 115–125 [in Japanese].

(16) W. Matsuda, A. Morikawa, A. Ohbuchi, T. Moriyama and T. Nakamura: *Anal. Sci.*, **36** (2020) 9, 1065–1070.

(17) H. Toda: *X-ray CT—Practical Application of Tomography in Industry, Science and Technology* (*X sen CT—Sangyo·Rikougaku deno Tomogurafii Jissen Katsuyou*), Kyoritsu Shuppan, Tokyo, (2019), 1–13 [in Japanese].

(18) H. Ishii: *J. Surf. Finish. Soc. Jpn* (*Hyomen Gijutsu*), **61** (2010) 3, 216–222 [in Japanese].

(19) G. K. Williamson and W. H. Hall: *Acta Metall*., **1** (1953), 22–31.

(20) H.-J. Bunge: *Texture Analysis in Materials Science–Mathematical Methods*, Transl. by Peter. R. Morris, Butterworths, London, (1982).

(21) K. Fujii and S. Takago: *Rept. Ind. Res. Inst. Ishikawa*, **54** (2004), https://www.irii.jp/randd/theme/h16/study03.htm.